Water isotopic characterisation of the cloud-circulation coupling in the North Atlantic trades. Part 2: The imprint of the atmospheric circulation at different scales

Leonie Villiger[1,2] and Franziska Aemisegger[1]

[1]Institute for Atmospheric and Climate Science, ETH Zurich, Zurich, Switzerland
[2]Institute for Environmental Decisions, ETH Zurich, Zurich, Switzerland

Correspondence: Leonie Villiger (leonie.villiger@env.ethz.ch)

Abstract. Water vapour isotopes reflect the history of moist atmospheric processes encountered by the vapour since evaporation from the ocean. This study focuses on water isotope variability in the winter trades near Barbados at cloud base, which has been identified as an important level for understanding the net radiative effects of shallow cumuli. The analyses are based on nested convection resolving COSMO$_{iso}$ simulations during the EUREC^{4}A field campaign. The two main findings are that (i) the contrasting isotope and humidity characteristics in clear-sky versus cloudy cloud base environments emerge due to vertical transport on time scales of 12 hours associated with local, convective circulations and show a clear diel cycle; and (ii) the cloud base isotopes are, in addition, sensitive to variations in the large-scale circulation on time scales of several days, which shows on average a Hadley-type subsidence but occasionally much stronger descent related to extratropical dry intrusions. This investigation, based on high-resolution isotope-enabled simulations in combination with trajectory analyses, reveals how dynamical processes at different scales act in concert to produce the observed humidity variations at the base of trade-wind cumuli.

1 Introduction

The response of shallow trade-wind clouds to climate change is uncertain and known to contribute substantially to the spread of climate projections (e.g., Bony et al., 2015; Zelinka et al., 2017). To shed light on the mechanisms controlling cloud fraction in the trades, the field campaign EUREC^{4}A (Stevens et al., 2021) was conducted in early 2020 near Barbados. The collected observations highlight the role of shallow mesoscale overturning circulations (George et al., 2022) in driving the variability of vertical velocities at cloud base, which is an important control of cloud fraction at this level (Vogel et al., 2022). It remains to be investigated how these overturning circulations, which have recently gained attention from the scientific community, shape the environment, particularly the distribution of humidity (Albright et al., 2022) and eventually cloud fraction.

Here, we are interested in using the abundance of heavy stable water vapour isotopologues as tracers of cloud microphysical processes, as well as turbulent and convective mixing. Heavy stable water vapour isotopologues (hereafter isotopes) are water molecules containing a heavy hydrogen ($^1H^2H^{16}O$) or oxygen atom ($^1H_2^{18}O$). Compared to their light counterpart ($^1H_2^{16}O$), they have lower saturation vapour pressures and lower diffusive velocities. This results in a change in the relative abundance

of heavy-to-light isotopes during phase transitions. The isotopic composition of a water sample is typically assessed with the
25   δ-value for ^{2}H and ^{18}O, respectively:

$$\delta^2\mathrm{H}\ [\text{‰}] = \left(\frac{^2R_{\mathrm{sample}}}{^2R_{\mathrm{VSMOW}}} - 1 \right) \cdot 1000 \tag{1}$$

$$\delta^{18}\mathrm{O}\ [\text{‰}] = \left(\frac{^{18}R_{\mathrm{sample}}}{^{18}R_{\mathrm{VSMOW}}} - 1 \right) \cdot 1000 \tag{2}$$

The R in the equations above stands for the atomic ratio of the concentration of the heavy to the light isotope, namely $^2R = $
30   $\frac{[^2\mathrm{H}]}{[^1\mathrm{H}]}$ and $^{18}R = \frac{[^{18}\mathrm{O}]}{[^{16}\mathrm{O}]}$, in the water sample and the internationally accepted Vienna Mean Ocean Standard Water 2 (VSMOW;
International Atomic Energy Agency, 2017). The relative variations of δ^2H and δ^{18}O is assessed with the deuterium excess:

$$\text{d-excess} = \delta^2\mathrm{H} - 8 \times \delta^{18}\mathrm{O} \tag{3}$$

which is a measure of the thermodynamic disequilibrium of the environment during phase transitions (e.g., Pfahl and Wernli,
2008). Due to these mechanisms, the abundance of heavy isotopes reflects the integral of all phase changes that occur along
35   the flow. While the first-order isotope parameter δ^2H is sensitive to microphysical processes and mixing (Gat, 1996; Galewsky
et al., 2016), the second-order isotope parameter d-excess is sensitive to the thermodynamic conditions at the moisture source
(Pfahl and Wernli, 2008; Aemisegger et al., 2021). Part 1 of this paper showed that the horizontal variability of humidity and
δ^2H of vapour at the cloud base emerges due to the cloud-relative circulation (Fig. 1a). Cloudy cloud base patches (representing
the ascending branch) are moister and more enriched than the background conditions. In contrast, clear-sky, dry-warm cloud
40   base patches (hereafter dry-warm patches; representing the descending branch) are drier and more depleted than the background
conditions. This suggests, against the above-formulated expectations, that the isotopic characteristics of the two cloud base
features mainly reflect vertical transport and are not primarily controlled by local microphysical or turbulent mixing processes.

In part 2 of this study, we establish a link between isotopes in the trade-wind region and characteristics of atmospheric
circulations. For this, we use three nested convection resolving COSMO$_{\mathrm{iso}}$ simulations with different resolutions and air parcel
45   backward trajectories from the cloud base environment. This data set and the applied methods are described in detail in Sect. 2.
First, we look at processes on the mesoscale (Sect. 3). We investigate how convection drives the variability of humidity and
isotopes in different cloud base environments (cloudy vs. dry-warm). Since convection in the trades has a clear diel cycle
(Vial et al., 2019; Vogel et al., 2020; Vial et al., 2021), we use it as a framework to answer the question: *Does the diel cycle
of humidity and δ^2H in different cloud base environments reflect the growth and decay of convection?* Second, we test the
50   hypothesis that the large-scale circulation transporting air into the trade-wind region leaves a distinct isotope signal in the
cloud base vapour (Sect. 4). We thus address the question: *Which of the three variables, specific humidity, δ^2H, and d-excess
is most strongly influenced by the large-scale circulation?* In the conclusion, we combine the findings from the two research
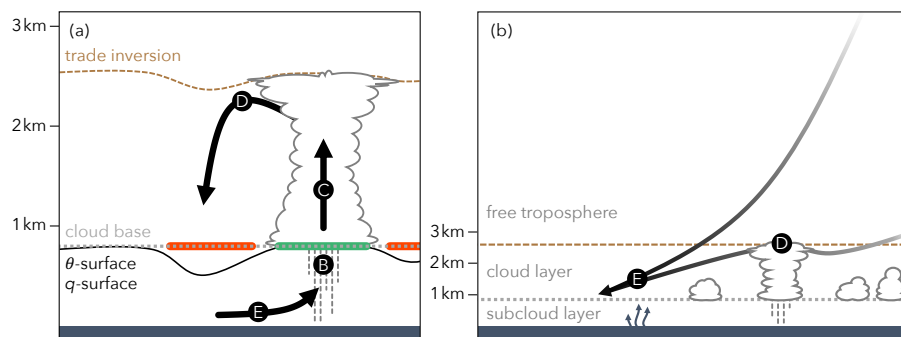questions (Sect. 5).

Figure 1. Idealised schematic of the processes affecting **(a)** the δ^2H in vapour within the overturning circulation associated with clouds, and **(b)** the d-excess in vapour during large-scale transport. Shown are three atmospheric layers, the subcloud layer, the cloud layer, and the free troposphere. They are separated by the cloud base level (dotted grey) and the trade inversion (dashed brown). It is assumed that the two boundaries have an uneven topography in reality. However, in the simulations cloud base is identified at a constant height. Therefore, the cloudy (thick green line in a) and the dry-warm (thick red line in a) cloud base environments are defined at the flat cloud base. **(a)** Within the cloud-relative circulation, air parcels (E) take up freshly evaporated and, therefore, isotopically heavy vapour from near the ocean surface; (B) may encounter below-cloud processes such as partial or full evaporation of hydrometeors and equilibration between vapour and liquid droplets, which can have a depleting or an enriching effect on the vapour; (C) will continuously lose heavy isotopes as soon as they reach the lifting condensation level and cloud and rain droplets are formed. Note that the temperature effect makes the fractionation stronger with increasing altitude. At any height, the now isotopically light air parcels may be detrained from the cloud into the surrounding clear-sky environment. Here, (D) the air parcels' vapour can get further depleted by mixing with vapour from above the trade inversion. **(b)** Within the large-scale circulation, air parcels can (E) take up moisture that is freshly evaporated from the ocean surface under non-equilibrium conditions and therefore has a relatively high d-excess (Pfahl and Wernli, 2008); (D) get moistened through the detrainment of cloudy air from precipitating clouds and have a comparatively low d-excess (Noone, 2012).

2 Data and methods

2.1 Applied datasets

The data from three convection-resolving COSMO$_{iso}$ simulations, described and evaluated in Villiger et al. (2023), are used. The simulations differ in terms of domain and horizontal grid spacing. They are referred to as COSMO$_{iso,1km}$, COSMO$_{iso,5km}$, and COSMO$_{iso,10km}$. COSMO$_{iso,1km}$ and COSMO$_{iso,5km}$ are used to characterise the cloud-relative circulation (Sect. 3), and COSMO$_{iso,10km}$ to assess the large-scale circulation (Sect. 4). For this, air parcel backward trajectories are calculated with data from COSMO$_{iso,5km}$ and COSMO$_{iso,10km}$ using the Lagrangian analysis tool Lagranto (Wernli and Davies, 1997; Sprenger and Wernli, 2015). Lagranto trajectories are based on the three-dimensional wind fields of the applied dataset, which do not resolve sub-grid scale boundary layer processes. To alleviate this limitation, we compute a large set of trajectories. Note also that the COSMO$_{iso,10km}$ trajectories spend comparably little of their lifetime near the boundary layer, and the COSMO$_{iso,5km}$

trajectory are explicitly started from features that are dominated by subsidence and expected to evolve at a speed resolved by the grid-scale winds.

2.2 Definition of cloud base

Cloud base is identified using the same procedure as in Villiger et al. (2023), i.e., with the following steps:

1. Every vertical profile in the domain 54.5-61° W and 11-16° N is checked for cloud water content exceeding $10\,\mathrm{mg\,kg^{-1}}$ (threshold for the detection of clouds used in Vial et al., 2019) at any model level below $1.3\,\mathrm{km}$. The lowest model level meeting this criterion is taken as the cloud base of the respective vertical profile. If the profile does not contain any clouds (i.e., does not meet the criteria), it is ignored in the subsequent step.

2. In order to extract cloud base conditions we determine one cloud base model level for the domain 54.5-61° W and 11-16° N by calculating the median over the cloud base model levels identified for cloudy profiles in the previous step.

3. Steps 1 and 2 are repeated for every hourly time step of the simulated time period. The resulting time series of cloud base model levels can then be used to extract cloud base variables from the $\mathrm{COSMO_{iso}}$ simulations.

The hourly cloud base levels alternate between 783 and $970\,\mathrm{m}$ for $\mathrm{COSMO_{iso,10km}}$ and 761, 914, and $1082\,\mathrm{m}$ for $\mathrm{COSMO_{iso,5km}}$ and $\mathrm{COSMO_{iso,1km}}$.

2.3 Definition of cloud base features

The $\mathrm{COSMO_{iso,1km}}$ and $\mathrm{COSMO_{iso,5km}}$ grid points at cloud base in the domain 54.5-61° W and 11-16° N are assigned to three categories representing features from the overturning circulation associated with clouds, clear-sky regions with dry-warm anomalies, and clear-sky regions of no particular interest (see details in Villiger et al., 2023, note that here we do not differentiate between precipitating and non-precipitating clouds and only take the vertical distribution of cloud water into account). The following definitions are applied to assign the data points:

- Cloudy grid points are identified through liquid cloud water content exceeding $10\,\mathrm{mg\,kg^{-1}}$. They are further stratified into shallow, middle, and deep clouds (size of categories in Fig. 5a) depending on their cloud top pressure ($p_{\mathrm{cloud\,top}}$) identified as the lowest pressure level in the vertical profile with liquid water exceeding $0\,\mathrm{mg\,kg^{-1}}$ (we relax the cloud criteria for cloud tops compared to cloud bases because we want to identify decaying clouds as well). More precisely:

    - shallow clouds have a $p_{\mathrm{cloud\,top}}$ larger than $800\,\mathrm{hPa}$,
    - middle clouds have a $p_{\mathrm{cloud\,top}}$ between 800 and $750\,\mathrm{hPa}$,
    - and deep clouds have a $p_{\mathrm{cloud\,top}}$ between 750 and $500\,\mathrm{hPa}$.

There are negligible ($< 1\,\%$) of the clouds that remain unclassified (i.e., have a $p_{\mathrm{cloud\,top}}$ above $500\,\mathrm{hPa}$).
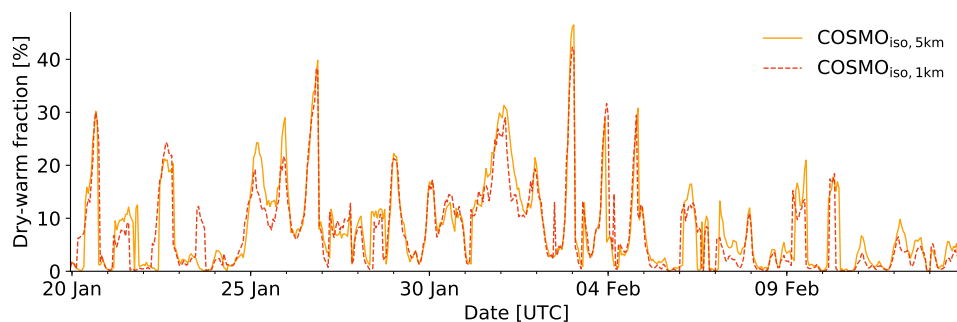
Figure 2. Hourly time series of fraction of cloud base grid points in the domain 54.5-61° W and 11-16° N with cloud liquid water exceeding $10\,\mathrm{mgkg}^{-1}$ in COSMO$_\mathrm{iso,5km}$ and COSMO$_\mathrm{iso,1km}$ (red dashed). The total number of cloud base grid points in the considered domain are 12632 for COSMO$_\mathrm{iso,5km}$, and 316028 for COSMO$_\mathrm{iso,1km}$.

– Dry-warm grid points are identified by a positive anomaly in potential temperature (θ) and a negative anomaly in specific humidity (q). The anomalies are defined grid-point-wise by removing the daily cycle. For each grid point, the hour-of-the-day mean and standard deviation are calculated over the whole simulated period (20 January to 13 February 2020). Dry-warm grid points are then selected using the following criteria: $q_{i,t} < \overline{q_{i,h(t)}} - \sigma(q_{i,h(t)})$ and $\theta_{i,t} < \overline{\theta_{i,h(t)}} + \sigma(\theta_{i,h(t)})$ (i standing for the grid points inside the evaluation domain, t for the hourly time steps of the simulated period, $h(t)$ for the hour of the day corresponding to the time step t). We checked that these criteria exclusively select clear-sky grid points (i.e., liquid cloud water content below $10\,\mathrm{mg\,kg}^{-1}$) without using an additional criterion for the liquid cloud water content. An overview of the number of identified dry-warm grid points per time step is given in Fig. 2 and an exemplary time step illustrating their spatial distribution in Fig. 3.

– The remaining clear-sky grid points (i.e., liquid cloud water content below $10\,\mathrm{mg\,kg}^{-1}$, but no positive anomaly in θ and no negative anomaly in q) belong to the clear-sky regions of no particular interest.

2.4 Subsidence in the cloud-relative circulation

To assess the subsidence rate of the mesoscale features that form the dry-warm patches at cloud base, we calculate 48 h-backward trajectories starting from the dry-warm cloud base grid points identified in COSMO$_\mathrm{iso,5km}$ (e.g., the red dots shown in Fig. 3d). The backward trajectories are started every hour from 22 January to 13 February 2020. The mean 1-h change of altitude ($\overline{\Delta z}$; Fig. 4b) for different time windows for each trajectory is used as a measure of the air parcel's vertical velocity. The mean vertical velocity of all air parcels arriving at cloud base at a given time step is, in most cases, negative. Therefore, we refer to it as the subsidence rate.
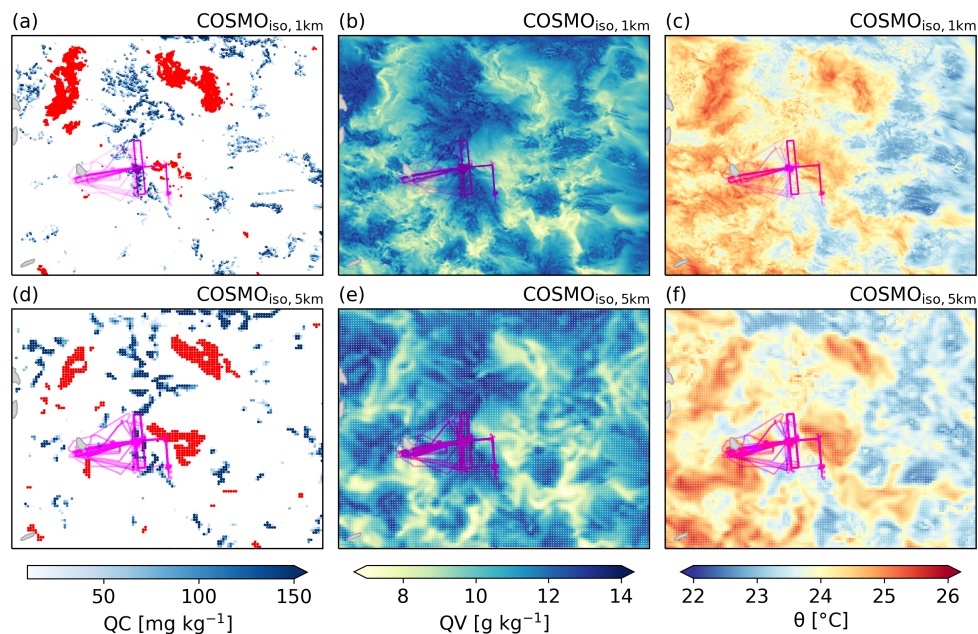
Figure 3. Spatial distribution of **(a,d)** cloud base grid points identified as dry-warm and cloud liquid water (QC), **(b,e)** specific humidity (QV), and **(c,f)** potential temperature (θ) at cloud base at 15 UTC on 2 February 2020. Shown is the data from **(a-c)** COSMO$_{iso,1km}$ and **(d-f)** COSMO$_{iso,1km}$ in the domain 54.5-61° W and 11-16° N. The fraction of grid points in the domain identified as dry-warm is **(a)** 3.27 % and **(b)** 4.32 %.

2.5 Subsidence in the large-scale circulation

We calculate trajectories based on COSMO$_{iso,10km}$ data to evaluate the role of the large-scale circulation for the isotopic composition of vapour around cloud base in Sect. 4. A total of 138 Lagranto trajectories, reaching 6 d backwards in time, are started every hour from 22 January to 13 February 2020, which is sufficient to capture the influence of a large-scale signal. The starting points are distributed over three vertical levels and horizontally spaced with a distance of 100 km in the domain 54.5-61° W and 11-16° N. The three vertical levels at 940, 920, and 900 hPa are chosen such that they bracket cloud base to take into account some variability in the cloud base level in the coarse resolution dataset. Hereafter, the air parcels' arrival level is referred to as cloud base. Furthermore, we do not distinguish between different cloud base mesoscale features (as in Sect. 2.3), because we expect the large-scale circulation to modulate isotope signals at the large-scale. Similarly to the trajectories calculated with the COSMO$_{iso,5km}$ data, we calculate the hourly net altitude change over different time windows for each trajectory ($\overline{\Delta z}$; Fig. 4b) and refer to the mean of this altitude change over all air parcels arriving at a given time step as subsidence rate.
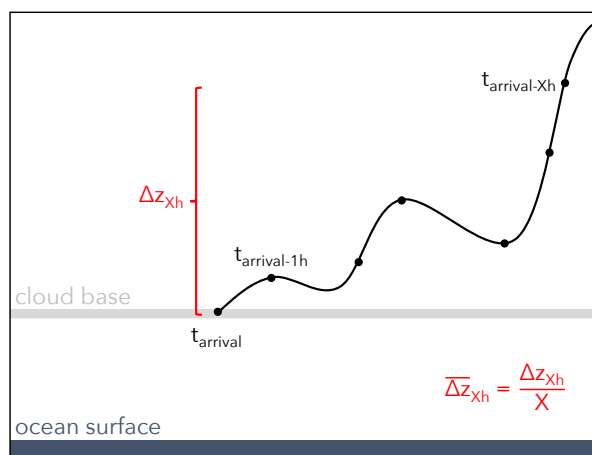
Figure 4. Schematic illustrating an individual backward trajectory in COSMO$_{iso,5km}$ or COSMO$_{iso,10km}$ started from cloud base and the procedure to obtain the mean altitude change ($\overline{\Delta z}$), which is used in the text as a measure for the subsidence rate.

3 Cloud base isotopes and the cloud-relative circulation

This section discusses how the cloud-relative circulation drives the diel cycle of isotopes in different cloud base environments (Fig. 5). For this, we select the cloud base data points from COSMO$_{iso,1km}$ which classify as cloudy or dry-warm (Sect. 2.3) and assume that the two categories represent mesoscale aggregations of clouds (Stevens et al., 2020; Bony et al., 2020) and the clear-sky environments in-between. In addition, we use COSMO$_{iso,5km}$ trajectories to derive an estimate of the vertical motion in the subsiding branch of the cloud-relative circulation (Sect. 2.4). We use COSMO$_{iso,5km}$ for these trajectories because COSMO$_{iso,1km}$ has too small a domain to trace air parcels over several hours.

The cloud fraction at the cloud base is maximal at night, followed by a continuous decrease until reaching a minimum shortly after noon (Fig. 5a). The reduction of clouds at low levels is associated with a deepening of the clouds leading to a slight increase in higher-reaching clouds (Fig. 5a). The strongest convection is found from ~3 a.m. to ~10 a.m. local time (LT), when updrafts at cloud base are strongest (Fig. 5b) and precipitation is most intense (Fig. 5a). Similarly to the updrafts, the subsiding branch of the cloud-relative circulation ($\overline{\Delta z}$; Fig. 5b) also accelerates (becomes more negative) during the night and is most pronounced in the early morning. The driver of this nighttime convective strengthening is assumed to be the horizontal inhomogeneity in the longwave cooling (Gray and Jacobson, 1977; Randall et al., 1991; Vial et al., 2019).

The diel cycles of δ^2H and specific humidity at cloud base (Fig. 5c,d; d-e) are more pronounced for the dry-warm patches (amplitudes of ~4‰ and 1.6 g kg^{-1}) than for the cloudy patches (amplitudes of ~0.9‰ and 0.5 g kg^{-1}). While the cloudy gird points are largely unaffected by the diel cycle of convection (Fig. 5c), the dry-warm grid points reach their most depleted and driest state (Fig. 5d) shortly after noon when cloud base cloudiness is minimal, representing the end of a period with enhanced up- and downward motions.
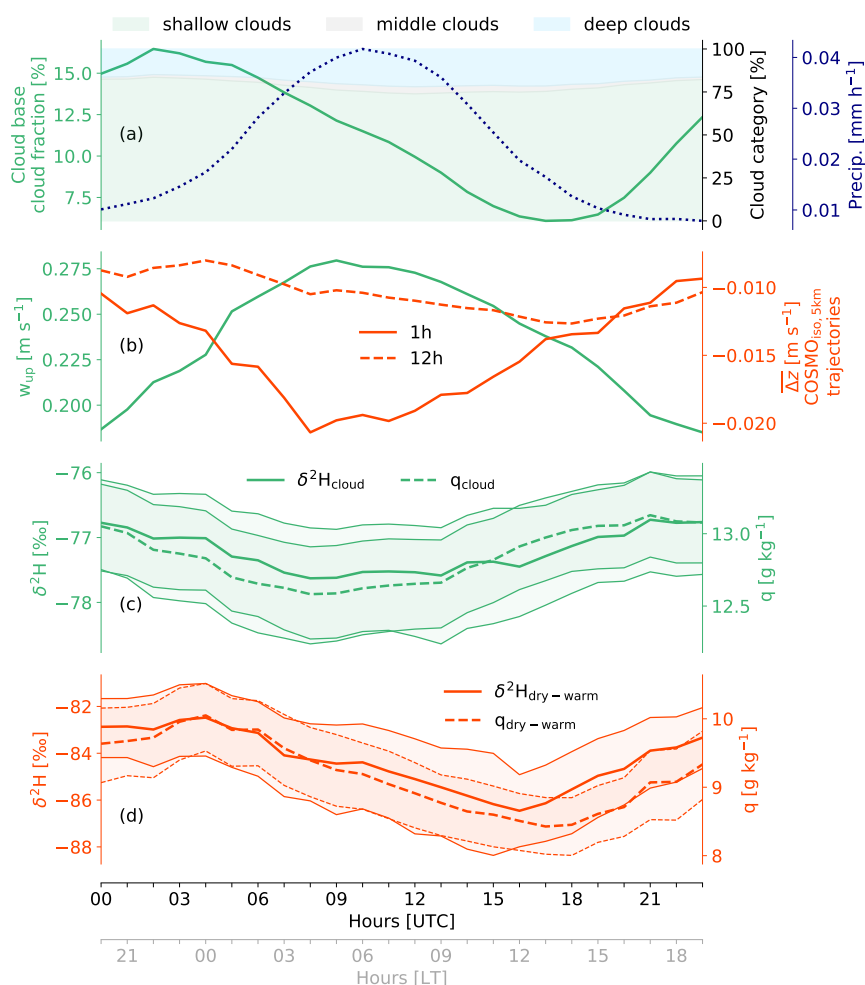
7

Figure 5. Diel cycle of **(a)** cloud fractions at the altitude of cloud base (continuous green), the fraction of the three cloud categories shallow/middle/deep (green/grey/blue shading; right black y-axis), and domain-averaged precipitation (dotted blue; right blue y-axis); **(b)** strength of updrafts at cloud base (mean of positive vertical velocities in cloudy grid points; w_{up}; continuous green) and subsidence of the air parcels arriving at cloud base in dry-warm patches (mean altitude change of $COSMO_{iso,5km}$ trajectories over the last 1 h [orange continuous] or 12 h [orange dashed] before arrival); **(c,d)** δ^2H in vapour with the median shown as a thick line and the 25-75-percentile range as shading/thin lines (continuous; left y-axis) and specific humidity (dashed; right y-axis) of **(c)** cloudy (green) and **(d)** dry-warm (orange) cloud base grid points. The hour-of-the-day mean values in the domain 54.5-61° W and 11-16° N during the period 20 January to 13 February 2020 are shown. Data: **(a-c)** $COSMO_{iso,1km}$ and **(b,** orange) $COSMO_{iso,5km}$ trajectories.

140　　Assuming an approximately closed overturning circulation, the depletion and drying of the dry-warm patches must be linked to the strengthening of convection. Two mechanisms likely contribute to the drying and depletion: (1) As an immediate effect, the decreasing cloud fraction reduces the moistening and enrichment of the dry-warm patches through lateral detrainment from surrounding clouds. (2) As a temporally delayed effect, the vertical growth of clouds has the consequence that the detrainment from clouds happens at increasing altitudes and, therefore, the amount of vapour that returns to the cloud base is less, and its

145　　isotope signal more depleted (due to continuous condensation and rainout in the convective updrafts). Evidence for the latter mechanism is the change in the subsidence rate. Since cloud base altitude is approximately constant (Villiger et al., 2023), more negative $\overline{\Delta z}$ indicates that the air parcels originate from higher altitudes (cf. analysis of Risi et al., 2019). But at which altitude does the detrainment happen?

　　The time interval between the minimum and maximum of the dry-warm patch characteristics (Fig. 5d) is 12 h. The 12-h

150　　subsidence (Fig. 5b) matches the diel cycle of the dry-warm patch characteristics: it is weakest ($-8\,\mathrm{mm\,s^{-1}}$) around 0 h LT when dry-warm patches are the moistest and most enriched and strongest ($-13\,\mathrm{mm\,s^{-1}}$) around 14 h LT when dry-warm patches are the driest and most depleted. The corresponding detrainment altitudes 12 h earlier are about 350 m and 560 m above cloud base, respectively.

　　In this section, we showed that at the hourly time scale, humidity and δ^2H at cloud base vary little inside clouds, while their

155　　variation in the dry-warm patches reflects the deepening of convection over the day, which (with a 12 h lag) causes drying and vapour depletion of the dry-warm patches. The information gained from humidity and δ^2H seems congruent, while the d-excess (not shown; Villiger, 2022) contains no signal of a diel cycle in any cloud base environment. Finally, we found evidence that the overturning circulation associated with clouds is only a few hundred meters deep.

4　Cloud base isotopes and the large-scale circulation

160 This section investigates which of the three variables, specific humidity, δ^2H, and d-excess, at the base of trade-wind clouds is most strongly influenced by the large-scale circulation. For this, we use trajectories based on the COSMO$_{\mathrm{iso,10km}}$ simulation (Sect. 2.5), which arrive evenly distributed near cloud base and are not targeted at cloudy or dry-warm patches. We use the mean subsidence rate ($\overline{\Delta z}$) to distinguish between large-scale circulation patterns. For Hadley-cell-like subsidence, resulting from the balance between radiative cooling and adiabatic warming, a rate of $\sim1.5\,\mathrm{hPa\,h^{-1}}$ (Salathé and Hartmann, 1997) is

165 expected. For air parcels that go through an extratropical dry intrusion before arriving in the trades (Aemisegger et al., 2021; Villiger et al., 2022), the subsidence of individual air parcels exceeds $\sim8\,\mathrm{hPa\,h^{-1}}$ (Raveh-Rubin, 2017).

　　The strongest links between the large-scale subsidence and the cloud base δ^2H and d-excess in the trades are found if the air parcels' pathway during 4 d and 6 d before arrival are considered, respectively (Table 1). The correlations are weaker for shorter or longer time scales, and the relationship is such that the vapour is more depleted and has a higher d-excess, the stronger the

170 subsidence of the air parcels. In comparison to the isotope parameters, humidity is not influenced by the large-scale subsidence (comparably low correlations with the maximum found at a short period; Table 1), illustrating the limited memory of moist processes registered by specific humidity alone.

Table 1. Pearson correlation coefficients between specific humidity (q), δ^2H in vapour, and d-excess in vapour of the COSMO$_{iso,10km}$ air parcels at their arrival near cloud base and their mean subsidence rate ($\overline{\Delta z}_{Xd}$; Sect. 2.5) during the 1/2/3/4/5/6 d before arrival. The correlations are calculated between the mean values of the 138 air parcels arriving every hour between 22 January and 13 February 2020. The strongest correlation for each variable is highlighted in italics. Data: COSMO$_{iso,10km}$.

	$\overline{\Delta z}_{Xd}$					
	1d	2d	3d	4d	5d	6d
q	0.29	*0.33*	0.19	0.05	0.07	0.13
δ^2H	0.3	0.54	0.63	*0.71*	0.57	0.43
d-excess	-0.16	-0.25	-0.37	-0.54	-0.72	*-0.75*

The physical link between the subsidence and δ^2H is straightforward: the stronger the subsidence, the isotopically lighter the vapour because it originates from higher altitudes. The link between the subsidence and the d-excess can be explained by the contrasting conditions at the site where the vapour is evaporated and picked up by the air parcels embedded in the large-scale circulation. Air parcels descending within an extratropical dry intrusion are expected to be drier and to create a stronger humidity gradient (increasing the d-excess) than air parcels crossing the North Atlantic at low levels within the comparably moist trade winds where frequent detrainment of cloudy air (lowering the d-excess; Fig. 1b) occurs.

The maximum correlation shown in Table 1 is slightly higher for the d-excess than for the δ^2H and negligible for humidity. Moreover, the period leading to the highest correlation extends further back for the d-excess than for δ^2H or humidity. Both findings suggest that of the three variables, the d-excess is most strongly influenced by the large-scale circulation. This meets expectations, as the d-excess is sensitive to the conditions at the moisture source (Pfahl and Wernli, 2008; Aemisegger et al., 2021) and less to subsequent cloud processes, which often happen under conditions close to equilibrium. Contrastingly, δ^2H is sensitive to equilibrium and non-equilibrium processes, meaning the source signal is more quickly overwritten than the one of d-excess.

The mean subsidence over all arrival time steps is $1.5\,\text{hPa}\,\text{h}^{-1}$ (Fig. 6), which corresponds to a Hadley-cell-like descent. However, the subsidence can be substantially stronger or weaker for individual time steps. To illustrate the variability in the large-scale circulation, four time steps with contrasting 6-d subsidence are selected (Fig. 7). The two cases with weaker subsidence (Fig. 7a,b) are associated with the typical zonal flow of the trades. In the two cases with stronger subsidence (Fig. 7c,d), the trades are interrupted by Rossby-wave breaking events over the central North Atlantic, which steer the air parcels from the extratropics towards low latitudes and cause a rapid descent along the slanted isentropes from the upper into the lower troposphere.
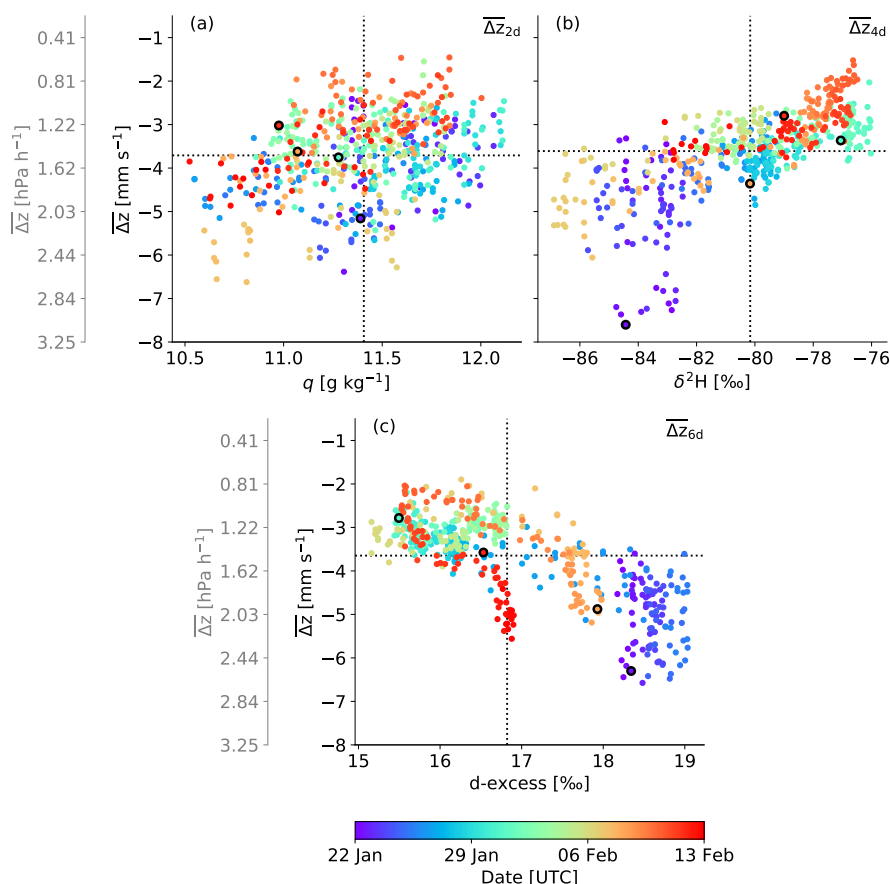
Figure 6. Relation between **(a)** specific humidity, **(b)** δ^2H in vapour, and **(c)** d-excess in vapour of the COSMO$_{iso,10km}$ air parcels at their arrival near cloud base and their mean subsidence rate ($\overline{\Delta z_{Xd}}$) over the period (Xd), which yielded the highest correlation (Table 1), i.e., 1, 4, and 6 d. The data points are coloured according to the arrival time step of the air parcels. Shown are the mean values over the 138 COSMO$_{iso,10km}$ air parcels arriving simultaneously (every hour from 22 January to 13 February 2020) at the three cloud base trajectory starting levels (940, 920, and 900 hPa) in the domain 54.5-61° W and 11-16° N. See Sect. 2 for details about how the subsidence is calculated. The dashed black lines indicate the mean values of the respective x- and y-variable over all arrival time steps. The data points with black borders represent arrival at 12 UTC on 22 January 2020, 15 UTC on 31 January 2020, 18 UTC on 8 February 2020, and 18 UTC on 12 February 2020. Data: COSMO$_{iso,10km}$.
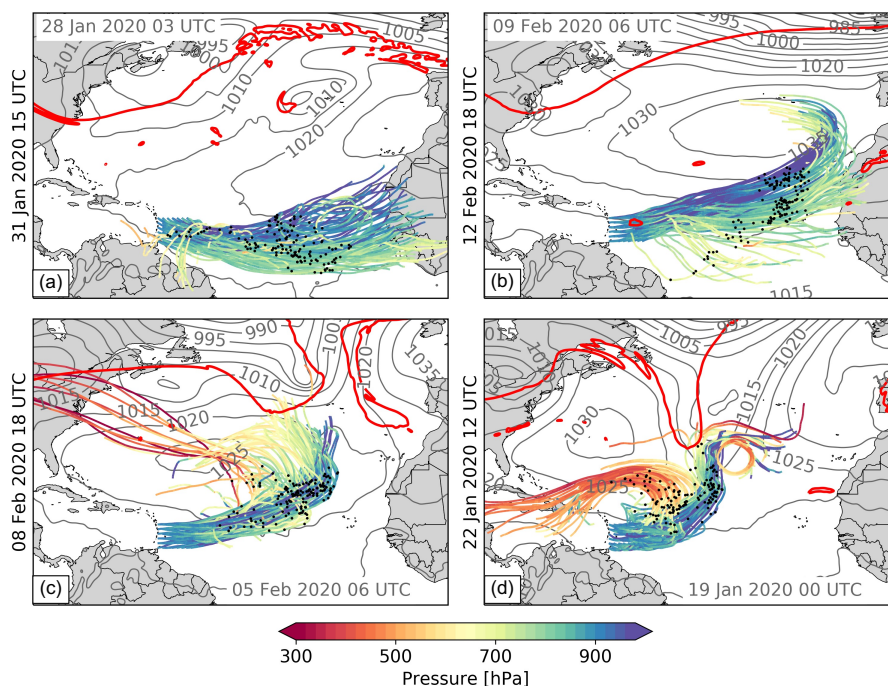
Figure 7. Exemplary time steps shown as black bordered markers in Fig. 6 illustrating the trajectories arriving at 940, 920, and 900 hPa in the domain 54.5-61° W and 11-16° N together with each air parcel's position (black dots), sea level pressure (grey contours), and the dynamical tropopause (2 pvu at 320 K; red contours) 3.5 d (date indicated in grey) before arrival. Shown is the domain 0-85° W and 5° S-55° N and the air parcels arriving **(a)** at 15 UTC on 31 January ($q = 11.3$ g kg^{-1}, δ^2H $= -77.1$‰, $d = 15.5$‰, 6-d subsidence $= -2.8$ mm s^{-1} or 1.1 hPa h^{-1}); **(b)** at 18 UTC on 12 February ($q = 11.0$ g kg^{-1}, δ^2H $= -79.0$‰, $d = 16.5$‰, 6-d subsidence $= -3.6$ mm s^{-1} or 1.5 hPa h^{-1}), **(c)** at 18 UTC on 8 February ($q = 11.1$ g kg^{-1}, δ^2H $= -80.2$‰, $d = 17.9$‰, 6-d subsidence $= -4.9$ mm s^{-1} or 2 hPa h^{-1}), and **(d)** at 12 UTC on 22 January 2020 ($q = 11.4$ g kg^{-1}, δ^2H $= -84.4$‰, $d = 18.3$‰, 6-d subsidence $= -6.3$ mm s^{-1} or 2.6 hPa h^{-1}). The dates are sorted according to the strength of the subsidence over 6 d, starting with the case with the weakest subsidence in (a). Data: COSMO$_{\text{iso,10km}}$.

5 Summary and conclusion

In this final section, we combine the insights from relating isotope signals at cloud base to the circulation at different scales.
First, we analysed the imprint of the cloud-relative circulation on cloud base water vapour isotopes in the trade-wind region.
We showed that the humidity and δ^2H in the vapour of cloudy cloud base patches remain largely unaffected by the vertical
growth of convection over the day. The dry-warm clear-sky cloud base patches, which are always drier and more depleted
than the cloudy patches, have a weak diel cycle linked to the cloud fraction at the cloud base and the cloud depth (i.e., the
detrainment altitude of the vapour from the clouds). The vertical growth of the clouds during the day lifts the detrainment
altitude. Correspondingly, the subsidence of the air parcels arriving in dry-warm patches at the cloud base is stronger for mass
conservation reasons. Specifically, the 12-h subsidence of the air parcels arriving in the dry-warm patches was identified as the
main control of the degree of drying and depletion. The information gained from humidity and δ^2H of the dry-warm patches
was largely congruent. However, by combining the two variables, we find a group of data points (Fig. 8a) that is shifted towards
lower δ^2H but shows no peculiarities in humidity or the 12-h subsidence. The stronger depletion of these data points signals
the influence of a large-scale process (Fig. 8b or extratropical intrusion discussed in Villiger et al., 2022).

Second, we showed that δ^2H and d-excess of the vapour near the cloud base (independently of the cloud base environment,
cloudy and dry-warm), but not humidity, vary on the synoptic scale following changes in the large-scale circulation in a
physically meaningful way. Namely, the vapour in the trade-wind region is more depleted and has a higher d-excess for
stronger subsidence rates during the preceding 4 to 6 d. The δ^2H in cloud base vapour was found to be most strongly linked to
the 4-d subsidence (Pearson correlation of 0.71), which also explains the more depleted data points in Fig. 8. Contrastingly, the
d-excess is most strongly linked to the 6-d subsidence (Pearson correlation of −0.75). The strong link between the d-excess
and the large-scale circulation found here is in agreement with Aemisegger et al. (2021, their Fig. 16), who found a clear link
(Pearson correlation of −0.73) between the d-excess in vapour measured on Barbados in the subcloud layer and the distance
to the moisture source, during a field experiment in early 2018. The analysis also showed that the identified pathways of air
parcels arriving in the lower troposphere qualitatively agree with the ones identified in Villiger et al. (2022).

To deepen our understanding of the hydrological cycle associated with shallow trade-wind cumulus clouds, the role of
mixing and liquid-vapour interaction processes embedded in the cloud-relative circulation should be examined in more detail.
Furthermore, a tagging experiment with numerical tracers distinguishing subcloud-layer and free-tropospheric moisture would
help to disentangle the contribution of the circulations associated with clouds of varying depths and the large-scale circulation.
Our analysis demonstrated that isotopes represent the integral signal of past moist atmospheric processes encountered along
the flow. Particularly novel was the finding that isotopes serve as indicators for changes in atmospheric circulations on various
scales. By investigating the isotope signal at cloud base in the trade-wind region, we could identify the imprint of different
large-scale circulation patterns and the overturning circulation associated with clouds that, in concert, determine the formation
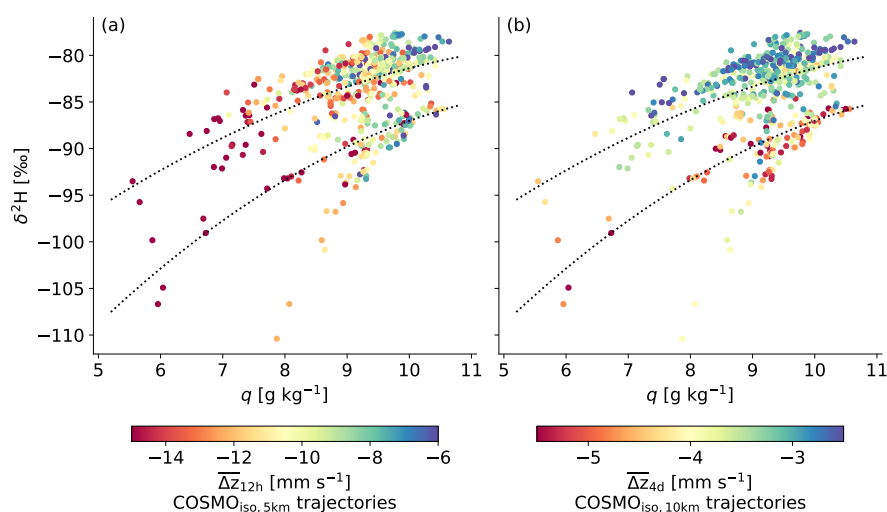of clouds and precipitation.

Figure 8. Relation between hourly median values of specific humidity (q) and δ^2H in the vapour of the cloud base grid points identified as dry-warm in the domain 54.5-61° W and 11-16° N from $COSMO_{iso,1km}$. They are coloured according to **(a)** $\overline{\Delta z}$ over 12 h from the $COSMO_{iso,5km}$ trajectories, and **(b)** $\overline{\Delta z}$ over 4 d from the $COSMO_{iso,10km}$ trajectories. The lines of two second-order polynomials are shown (dashed black) that were fitted to the data points with large-scale subsidence **(b)** stronger or weaker than $-4.5\,\mathrm{mm\,s^{-1}}$, respectively. See text in Sect. 3 and Sect. 4 for reasoning of the chosen time windows for $\overline{\Delta z}$.

References

Aemisegger, F., Vogel, R., Graf, P., Dahinden, F., Villiger, L., Jansen, F., Bony, S., Stevens, B., and Wernli, H.: How Rossby wave breaking
235   modulates the water cycle in the North Atlantic trade wind region, Weather Clim. Dynam., 2, 281–309, https://doi.org/10.5194/wcd-2-281-2021, 2021.

Albright, A. L., Bony, S., Stevens, B., and Vogel, R.: Observed subcloud layer moisture and heat budgets in the trades, J. Atmos. Sci., 79,
2363–2385, https://doi.org/10.1175/JAS-D-21-0337.1, 2022.

Bony, S., Stevens, B., Frierson, D. M., Jakob, C., Kageyama, M., Pincus, R., Shepherd, T. G., Sherwood, S. C., Siebesma, A. P., Sobel, A. H.,
240   Watanabe, M., and Webb, M. J.: Clouds, circulation and climate sensitivity, Nat. Geosci., 8, 261–268, https://doi.org/10.1038/ngeo2398,
2015.

Bony, S., Schulz, H., Vial, J., and Stevens, B.: Sugar, gravel, fish, and flowers: Dependence of mesoscale patterns of trade-wind clouds on
environmental conditions, Geophys. Res. Lett., 47, 1–9, https://doi.org/10.1029/2019GL085988, 2020.

Galewsky, J., Steen-Larsen, H. C., Field, R. D., Worden, J., Risi, C., and Schneider, M.: Stable isotopes in atmospheric water vapor and
245   applications to the hydrologic cycle, Rev. Geophys., 54, 809–865, https://doi.org/10.1002/2015RG000512, 2016.

Gat, J. R.: Oxygen and hydrogen isotopes in the hydrologic cycle, Annu. Rev. Earth Pl. Sc., 24, 225–262,
https://doi.org/10.1146/annurev.earth.24.1.225, 1996.

George, G., Stevens, B., Bony, S., Vogel, R., and Naumann, A. K.: Ubiquity of shallow mesoscale circulations in the trades and their influence
on moisture variance, Nat. Geosci. [preprint], https://doi.org/10.1002/essoar.10512427.1, 2022.

250   Gray, W. M. and Jacobson, R. W.: Diurnal-variation of deep cumulus convection, Mon. Weather Rev., 105, 1171–1188,
https://doi.org/10.1175/1520-0493(1977)105<1171:DVODCC>2.0.CO;2, 1977.

International Atomic Energy Agency: Reference Sheet for VSMOW2 and SLAP2 international measurement standards., IAEA, Vienna,
2017.

Noone, D.: Pairing measurements of the water vapor isotope ratio with humidity to deduce atmospheric moistening and dehydration in the
255   tropical midtroposphere, J. Climate, 25, 4476–4494, https://doi.org/10.1175/JCLI-D-11-00582.1, 2012.

Pfahl, S. and Wernli, H.: Air parcel trajectory analysis of stable isotopes in water vapor in the eastern Mediterranean, J. Geophys. Res.-
Atmos., 113, 1–16, https://doi.org/10.1029/2008JD009839, 2008.

Randall, D. A., Harshvardhan, and Dazlich, D. A.: Diurnal variability of the hydrologic-cycle in a general-circulation model, J. Atmos. Sci.,
48, 40–62, https://doi.org/10.1175/1520-0469(1991)048<0040:DVOTHC>2.0.CO;2, 1991.

260   Raveh-Rubin, S.: Dry intrusions: Lagrangian climatology and dynamical impact on the planetary boundary layer, J. Climate, 30, 6661–6682,
https://doi.org/10.1175/JCLI-D-16-0782.1, 2017.

Risi, C., Galewsky, J., Reverdin, G., and Brient, F.: Controls on the water vapor isotopic composition near the surface of tropical oceans and
role of boundary layer mixing processes, Atmos. Chem. Phys., 19, 12 235–12 260, https://doi.org/10.5194/acp-19-12235-2019, 2019.

Salathé, E. P. and Hartmann, D. L.: A trajectory analysis of tropical upper-tropospheric moisture and convection, J. Climate, 10, 2533–2547,
265   https://doi.org/10.1175/1520-0442(1997)010<2533:ATAOTU>2.0.CO;2, 1997.

Sprenger, M. and Wernli, H.: The LAGRANTO Lagrangian analysis tool - Version 2.0, Geosci. Model Dev., 8, 2569–2586,
https://doi.org/10.5194/gmd-8-2569-2015, 2015.

Stevens, B., Bony, S., Brogniez, H., Hentgen, L., Hohenegger, C., Kiemle, C., L'Ecuyer, T. S., Naumann, A. K., Schulz, H., Siebesma, P. A., Vial, J., Winker, D. M., and Zuidema, P.: Sugar, gravel, fish and flowers: Mesoscale cloud patterns in the trade winds, Q. J. Roy. Meteor. Soc., 146, 141–152, https://doi.org/10.1002/qj.3662, 2020.

Stevens, B., Bony, S., Farrell, D., Ament, F., Blyth, A., Fairall, C., Karstensen, J., Quinn, P., Speich, S., Aemisegger, F., Albright, A., Bodenschatz, E., Chewitt-Lucas, R., Delanoë, J., Ewald, F., Forde, M., George, G., Hausold, A., Hagen, M., Hirsch, L., Jansen, F., Kinne, S., Klocke, D., Kölling, T., Konow, H., Mohr, W., Naumann, A., Nuijens, L., Pincus, R., Reverdin, G., Roberts, G., Schnitt, S., Sullivan, P., Touzé-Peiffer, L., Vial, J., Vogel, R., Acquistapace, C., Alexander, N., Alves, L., Arixi, S., Asmath, H., Bagheri, G., Bailey, A., Baranowski, D., Baron, A., Barrau, S., Barrett, P., Behrendt, A., Bellenger, H., Bendinger, A., Beucher, F., Bigorre, S., Blossey, P., Bock, O., Bosser, P., Bourras, D., Bouruet-Aubertot, P., Bower, K., Branger, H., Brennek, M., Brewer, A., Brügmann, B., Buehler, S., Burke, E., Burton, R., Böing, S., Calmer, R., Carton, X., Cato, G., Charles, J., Chazette, P., Chen, Y., Choularton, T., Chuang, P., Clarke, S., Coe, H., Cornet, C., Coutris, P., Couvreux, F., Crewell, S., Cronin, T., Cui, Z., Cuypers, Y., Daley, A., Damerell, G., Dauhut, T., Denby, L., Deneke, H., Douet, V., Drushka, K., Dütsch, M., Ehrlich, A., Emanuel, K., Emmanouilidis, A., Etienne-Leblanc, S., Faure, G., Feingold, G., Ferrero, L., Fildier, B., Fix, A., Flamant, C., Flatau, P., Foltz, G., Gadian, A., Galewsky, J., Gallagher, M., Gallimore, P., Gaston, C., Gentemann, C., Geyskens, N., Giez, A., Gourbeyre, C., Gross, S., Grosz, R., Gutleben, M., Güttler, J., Hall, K., Harris, G., Helfer, K., Henze, D., Herbert, C., Heywood, K., Holanda, B., Ibanez-Landeta, A., Intrieri, J., Iyer, S., Jacob, M., Julien, F., Kalesse, H., Kazil, J., Kellman, A., Kirchner, U., Klingebiel, M., Kremper, L., Kretzschmar, J., Krüger, O., Kurz, A., Körner, M., Lachlan-Cope, T., Laing, A., Landschützer, P., Lang, T., Lange, D., Lange, I., Laplace, C., Laxenaire, R., Leandro, M., Lefevre, N., Lenschow, D., Li, Q., Lloyd, G., Los, S., Losi, N., Lothon, M., Lovell, O., Luneau, C., Makuch, P., Malinowski, S., Manta, G., Marinou, E., Marsden, N., Matthieu, L., Maury, N., Mayer, B., Mayers-Als, M., Mazel, C., Mcgeary, W., Mcwilliams, J., Mech, M., Mehlmann, M., Meroni, A., Mieslinger, T., Minikin, A., Muller, C., Musat, I., Möller, G., Napoli, A., Neuberger, A., Noone, D., Nordsiek, F., Nowak, J., Olivier, L., Oswald, L., Parker, D., Peck, C., Person, R., Plueddemann, A., Pologne, L., Posyniak, M., Prange, M., Pöhlker, M., Pöhlker, C., Pörtge, V., Pöschl, U., Radtke, J., Ramage, K., Reimann, J., Renault, L., Reus, K., Reyes, A., Ribbe, J., Ringel, M., Ritschel, M., Rocha, C., Rochetin, N., Rollo, C., Röttenbacher, J., Saffin, L., Sandiford, S., Sandu, I., Schemann, V., Schirmacher, I., Schlenczek, O., Schmidt, J., Schröder, M., Schulz, H., Schwarzenboeck, A., Schäfer, M., Sealy, A., Serikov, I., Shohan, S., Siddle, E., Siebesma, A., Späth, F., Stephan, C., Stolla, M., Szkółka, W., Tarot, S., Tetoni, E., Thompson, E., Thomson, J., Tomassini, L., Totems, J., Villiger, L., Walther, A., Webber, B., Wendisch, M., Whitehall, S., Wiltshire, A., Wing, A., Wirth, M., Wiskandt, J., Wolf, K., Worbes, L., Wright, E., Wulfmeyer, V., Young, S., Zhang, D., Zhang, C., Ziemen, F., Zinner, T., Zuidema, P., and Zöger, M.: EUREC4A, Earth Syst. Sci. Data, 13, 4067–4119, https://doi.org/10.5194/essd-13-4067-2021, 2021.

Vial, J., Vogel, R., Bony, S., Stevens, B., Winker, D. M., Cai, X., Hohenegger, C., Naumann, A. K., and Brogniez, H.: A new look at the daily cycle of tradewind cumuli, J. Adv. Model. Earth Sy., 11, 3148–3166, https://doi.org/10.1029/2019ms001746, 2019.

Vial, J., Vogel, R., and Schulz, H.: On the daily cycle of mesoscale cloud organization in the winter trades, Q. J. Roy. Meteor. Soc., 147, 2850–2873, https://doi.org/10.1002/qj.4103, 2021.

Villiger, L.: Large-scale circulation drivers and stable water isotope characteristics of shallow clouds over the tropical North Atlantic, Ph.D. thesis, ETH Zürich, https://doi.org/10.3929/ethz-b-000586270, 2022.

Villiger, L. and Aemisegger, F.: Numerical weather simulation using COSMOiso over the tropical North Atlantic in January and February 2020 in the context of EUREC4A, ETH Research Collection, https://doi.org/10.3929/ethz-b-000584213, 2022.

Villiger, L., Wernli, H., Boettcher, M., Hagen, M., and Aemisegger, F.: Lagrangian formation pathways of moist anomalies in the trade-wind region during the dry season: two case studies from EUREC4A, Weather Clim. Dynam., 3, 59–88, https://doi.org/10.5194/wcd-3-59-2022, 2022.

Villiger, L., Dütsch, M., Bony, S., Lothon, M., Pfahl, S., Wernli, H., Brilouet, P.-E., Chazette, P., Coutris, P., Delanoë, J., Flamant, C., Schwarzenboek, A., Werner, M., and Aemisegger, F.: Water isotopic characterisation of the cloud-circulation interaction in the North Atlantic trades. Part 1: A process-oriented evaluation of COSMOiso simulations with EUREC4A observations, In preparation for Atmos. Chem. Phys., 2023.

Vogel, R., Bony, S., and Stevens, B.: Estimating the shallow convective mass flux from the subcloud-layer mass budget, J. Atmos. Sci., 77, 1559–1574, https://doi.org/10.1175/JAS-D-19-0135.1, 2020.

Vogel, R., Albright, A. L., Vial, J., George, G., Stevens, B., and Bony, S.: Strong cloud-circulation coupling explains weak trade cumulus feedback, Nature, 612, 696–700, https://doi.org/10.1038/s41586-022-05364-y, 2022.

Wernli, H. and Davies, H. C.: A Lagrangian-based analysis of extratropical cyclones. I: The method and some applications, Q. J. Roy. Meteor. Soc., 123, 467–489, https://doi.org/10.1256/smsqj.53810, 1997.

Zelinka, M. D., Randall, D. A., Webb, M. J., and Klein, S. A.: Clearing clouds of uncertainty, Nat. Clim. Change, 7, 674–678, https://doi.org/10.1038/nclimate3402, 2017.